AIMS Mathematics, 9(8): 22665–22679.
DOI:10.3934/math.20241104
Received: 07 May 2024
Revised: 08 July 2024
Accepted: 10 July 2024
Published: 22 July 2024

http://www.aimspress.com/journal/Math

Research article

Real-time detection of small objects in transverse electric polarization: Evaluations on synthetic and experimental datasets

Junyong Eom[1] **and Won-Kwang Park**[2,*]

[1] Research Institute for Electronic Science, Hokkaido University, Sapporo, 001-0020, Japan

[2] Department of Information Security, Cryptography, and Mathematics, Kookmin University, Seoul, 02707, Korea

* **Correspondence:** Email: parkwk@kookmin.ac.kr.

Abstract: It is well-known that if one applies Kirchhoff migration (KM) to identify small objects when their values of magnetic permeabilities differ from those of the background (or transverse electric polarization), their location and outline shape cannot be satisfactorily retrieved because rings of large magnitudes centered at the location of objects appear in the imaging results. Fortunately, it is possible to recognize the existence and approximated location of objects in the 2D Fresnel dataset through the traditional KM, but no theoretical explanation for this phenomenon has been verified. Here we show that the imaging function of KM when tested on the Fresnel dataset can be expressed as squared zero-order and first-order Bessel functions and as an infinite series of Bessel functions of integer order greater than two. We also explain why the existence and approximate location of objects can be identified. This theoretical result is supported by numerical simulations on synthetic and experimental data.

Keywords: Bessel function; Kirchhoff migration; numerical simulations; transverse electric polarization
Mathematics Subject Classification: 78A46

1. Introduction

We consider the limited-aperture inverse scattering problem for fast identification of the existence and location of a set of two-dimensional (2D) small objects from measured scattered field data. Previous researchers have developed various imaging techniques, including the bifocusing method for identifying small objects in inverse scattering problem [1], in microwave imaging [2], and damage detection of concrete void [3], the direct sampling method to localize 2D small inhomogeneities with multi- [4] and mono- [5] measurement environments, and perfectly conducting cracks [6], the

MUltiple SIgnal Classification (MUSIC) algorithm for localizing small objects buried in a half-space [7], microwave imaging [8], and limited-aperture inverse scattering problem [9], Kirchhoff and subspace migration techniques to retrieve small cracks with measurements placed on a line [10], curve-like perfectly conducting cracks [11], and small anomalies from limited-aperture measurements in real-world microwave imaging [12], topological derivatives for inversion of Fresnel databases [13], multi-frequency limited data [14], and shape reconstruction of thin, curve-like inhomogeneities [15], the linear sampling method for identifying unknown scatterers from limited-aperture measurement data [16] and experimental dataset [17], and breast cancer detection [18], and the orthogonality sampling method for localizing unknown objects from experimental dataset [19], 3D far-field pattern data [20], and scattering parameter data [21]. We also refer to several references [22–27] about fast imaging techniques.

Although these techniques are fast, effective, and robust, they are typically designed for the detection of objects with dielectric permittivities that differ from the background value; the detection of objects with different magnetic permeabilities from the background permeability has been comparatively neglected. We refer to [28–32] for related studies. These studies report that rings with large magnitudes centered at the location of small objects appear in the imaging results. However, unlike the previous studies, peaks of large magnitude appear at the location of small objects with the Fresnel dataset. Thus, it is possible to recognize the existence and approximate locations of small objects. However, the theoretical reason for this phenomenon has not been explored.

Motivated by the above problem, we apply KM with a limited-aperture experimental measurement configuration [33] for a fast identification of small objects with different magnetic permeabilities from the background value. To validate object detection, we show that the imaging function of the KM can be expressed in terms of the size and permeability of the objects, squared zero-order and first-order Bessel functions, and an infinite series of Bessel functions of integer order greater than two. This is based on the fact that measured scattered field can be modeled as a 2D scalar Helmholtz equation and represented by an asymptotic expansion formula. The identified structure reveals some properties of the KM and explains some phenomena, such as object detectability.

The remainder of this study is structured as follows: Section 2 briefly introduces the 2D forward problem in the presence of small objects and the asymptotic expansion formula of the scattered field. Section 3 introduces and analyzes the imaging function, and explains some properties of the imaging results. Section 4 exhibits numerical simulation results with synthetic and Fresnel experimental data to support the theoretical results. Section 5 briefly concludes the paper and proposes future research.

2. Forward problem and the asymptotic expansion formula

Here, we briefly introduce the forward problem and the asymptotic expansion formula of the scattered field when a set of small circular objects is completely embedded in a homogeneous region $\Omega \subset \mathbb{R}^2$. These objects with radii of α_s at locations $\mathbf{r}_s$ are denoted as D_s, $s = 1, 2, \cdots, S$, and all D_s are assumed to be well separated. Let D be the collection of D_s and based on the simulation configuration in [33], the values of the background conductivity, magnetic permeability, and dielectric permittivity are $\sigma_\mathrm{b} \approx 0$, $\mu_\mathrm{b} = 4\pi \times 10^{-7}\,\mathrm{H/m}$, and $\varepsilon_\mathrm{b} = 8.854 \times 10^{-12}\,\mathrm{F/m}$, respectively, at a given angular frequency ω. Additionally, we denote $k_\mathrm{b} = \omega\sqrt{\varepsilon_\mathrm{b}\mu_\mathrm{b}}$ as the background wavenumber.

In this paper, we assume that every material is characterized by its value of permeability at ω.

Denoting μ_s as the permeability of D_s, we introduce the piecewise constant of magnetic permeability

$$\mu(\mathbf{r}) = \begin{cases} \mu_s & \text{if} \quad \mathbf{r} \in D_s \\ \mu_{\mathrm{b}} & \text{if} \quad \mathbf{r} \in \Omega \backslash \overline{D}. \end{cases}$$

Let $\mathcal{A}_m$, $m = 1, 2, \ldots, M$, and $\mathcal{B}_n$, $n = 1, 2, \ldots, N$, be the mth transmitter and nth receiver located at $\mathbf{a}_m$ and $\mathbf{b}_n$, respectively. Based on [33], antennas $\mathcal{A}_m$ and $\mathcal{B}_n$ are placed on the circles with radii of 0.72 m and 0.76 m, respectively. The transmitters $\mathcal{A}_m$ are uniformly distributed with step sizes of $\triangle\vartheta = \pi/18$ from 0 to $35\pi/18$, and at each location of $\mathcal{A}_m$, the receivers $\mathcal{B}_n$ are uniformly distributed with step sizes of $\triangle\theta = \pi/36$ from $\pi/3$ to $5\pi/3$. For an illustration of the simulation configuration, we refer to Figure 1. Then, the locations of $\mathbf{a}_m$ and $\mathbf{b}_n$ are given by

$$\mathbf{a}_m = |\mathbf{a}_m|\boldsymbol{\vartheta}_m = 0.72\,\mathrm{m}(\cos\vartheta_m, \sin\vartheta_m), \quad \vartheta_m = (m-1)\triangle\vartheta$$

and

$$\mathbf{b}_n = |\mathbf{b}_n|\boldsymbol{\theta}_n = 0.76\,\mathrm{m}(\cos\theta_n, \sin\theta_n), \quad \theta_n = (n-1)\triangle\theta,$$

respectively.

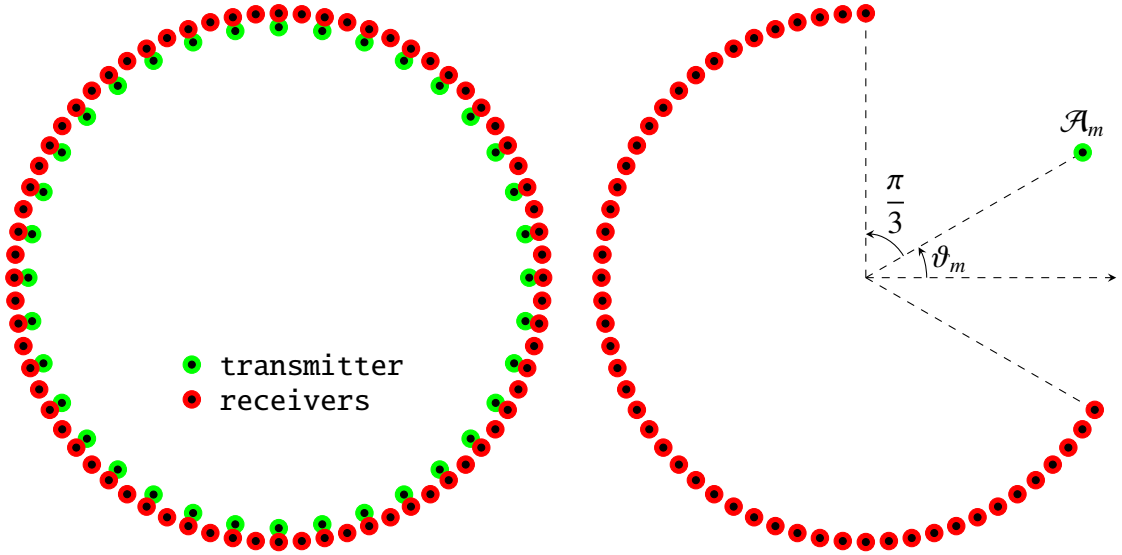

Figure 1. Transmitter and receiver arrangements.

With this setting, the incident field generated at $\mathcal{A}_m$ is given by

$$u_{\mathrm{inc}}(\mathbf{r}, \mathbf{a}_m) = -\frac{i}{4}H_0^{(1)}(k_{\mathrm{b}}|\mathbf{r} - \mathbf{a}_m|) = G(\mathbf{r}, \mathbf{a}_m),$$

where $H_0^{(1)}$ denotes the zero-order Hankel function of the first kind. Assuming a time dependence of $e^{-i\omega t}$, the time-harmonic total field $u(\mathbf{b}_n, \mathbf{r})$ measured at $\mathcal{B}_n$ satisfies

$$\begin{cases} \nabla \cdot \left(\dfrac{1}{\mu(\mathbf{r})}\nabla u(\mathbf{b}_n, \mathbf{r})\right) + \omega^2 \varepsilon_{\mathrm{b}} u(\mathbf{b}_n, \mathbf{r}) = 0 \quad \text{in} \quad \Omega \\ \dfrac{1}{\mu_s}\dfrac{\partial u(\mathbf{b}_n, \mathbf{r})}{\partial \nu(\mathbf{r})}\bigg|_- - \dfrac{1}{\mu_{\mathrm{b}}}\dfrac{\partial u(\mathbf{b}_n, \mathbf{r})}{\partial \nu(\mathbf{r})}\bigg|_+ = 0 \quad \text{on} \quad \partial D_s, \ s = 1, 2, \ldots, S. \end{cases}$$

Let $u_{\text{scat}}(\mathbf{r}, \mathbf{a}_m) = u(\mathbf{r}, \mathbf{a}_m) - u_{\text{inc}}(\mathbf{r}, \mathbf{a}_m)$ be the measured scattered field data at $\mathbf{r}$ in the presence of D that satisfies the outgoing wave condition (or Sommerfeld radiation condition)

$$\left| \frac{\mathrm{d}u_{\text{scat}}(\mathbf{r}, \mathbf{a}_m)}{\mathrm{d}r} - ik_{\text{b}} u_{\text{scat}}(\mathbf{r}, \mathbf{a}_m) \right| = o\left(\frac{1}{\sqrt{r}}\right)$$

uniformly in all directions $\frac{\mathbf{r}}{|\mathbf{r}|}$ as $r \longrightarrow \infty$. Based on [34], $u_{\text{scat}}(\mathbf{b}_n, \mathbf{a}_m)$ can be expressed as the double-layer potential

$$u_{\text{scat}}(\mathbf{b}_n, \mathbf{a}_m) = \int_D \frac{\partial G(\mathbf{b}_n, \mathbf{r})}{\partial \boldsymbol{\nu}(\mathbf{r})} \psi(\mathbf{r}, \mathbf{a}_m) d\mathbf{r} = \sum_{s=1}^{S} \int_{D_s} \frac{\partial G(\mathbf{b}_n, \mathbf{r})}{\partial \boldsymbol{\nu}(\mathbf{r})} \psi(\mathbf{r}, \mathbf{a}_m) d\mathbf{r},$$

where ψ is an unknown density function. We emphasize that, as the complete form of ψ is unknown, it must be replaced with an alternative expression to design an imaging function. Due to this reason, we consider the following asymptotic expansion formula (see [35]) to introduce and analyze the imaging function.

Lemma 2.1 (Asymptotic formula)**.** *If α_s, $s = 1, 2, \ldots, S$ is small, the scattered field $u_{\text{scat}}(\mathbf{b}_n, \mathbf{a}_m)$ can be represented as*

$$u_{\text{scat}}(\mathbf{b}_n, \mathbf{a}_m) = \sum_{s=1}^{S} \alpha_s^2 \pi \left(\frac{\mu_{\text{b}}}{\mu_s + \mu_{\text{b}}} \right) \nabla G(\mathbf{b}_n, \mathbf{r}_s) \cdot \nabla G(\mathbf{a}_m, \mathbf{r}_s) + o(\alpha_s^2). \tag{2.1}$$

3. Introduction and analysis of the imaging function

This section introduces the imaging function for D_s identification and analyzes its structure to elucidate its various properties. To this end, assume that we can handle the following multi-static response (MSR) matrix:

$$\mathbb{K} = \begin{pmatrix} u_{\text{scat}}(\mathbf{b}_1, \mathbf{a}_1) & u_{\text{scat}}(\mathbf{b}_1, \mathbf{a}_2) & \cdots & u_{\text{scat}}(\mathbf{b}_1, \mathbf{a}_M) \\ u_{\text{scat}}(\mathbf{b}_2, \mathbf{a}_1) & u_{\text{scat}}(\mathbf{b}_2, \mathbf{a}_2) & \cdots & u_{\text{scat}}(\mathbf{b}_2, \mathbf{a}_M) \\ \vdots & \vdots & \ddots & \vdots \\ u_{\text{scat}}(\mathbf{b}_N, \mathbf{a}_1) & u_{\text{scat}}(\mathbf{b}_N, \mathbf{a}_2) & \cdots & u_{\text{scat}}(\mathbf{b}_N, \mathbf{a}_M) \end{pmatrix}. \tag{3.1}$$

Using (2.1), $\mathbb{K}$ can be represented as

$$\mathbb{K} \approx \sum_{s=1}^{S} \frac{\alpha_s^2 \mu_{\text{b}} \pi}{\mu_s + \mu_{\text{b}}} \begin{pmatrix} \nabla G(\mathbf{b}_1, \mathbf{r}_s) \cdot \nabla G(\mathbf{a}_1, \mathbf{r}_s) & \nabla G(\mathbf{b}_1, \mathbf{r}_s) \cdot \nabla G(\mathbf{a}_2, \mathbf{r}_s) & \cdots & \nabla G(\mathbf{b}_1, \mathbf{r}_s) \cdot \nabla G(\mathbf{a}_M, \mathbf{r}_s) \\ \nabla G(\mathbf{b}_2, \mathbf{r}_s) \cdot \nabla G(\mathbf{a}_1, \mathbf{r}_s) & \nabla G(\mathbf{b}_2, \mathbf{r}_s) \cdot \nabla G(\mathbf{a}_2, \mathbf{r}_s) & \cdots & \nabla G(\mathbf{b}_2, \mathbf{r}_s) \cdot \nabla G(\mathbf{a}_M, \mathbf{r}_s) \\ \vdots & \vdots & \ddots & \vdots \\ \nabla G(\mathbf{b}_N, \mathbf{r}_s) \cdot \nabla G(\mathbf{a}_1, \mathbf{r}_s) & \nabla G(\mathbf{b}_N, \mathbf{r}_s) \cdot \nabla G(\mathbf{a}_2, \mathbf{r}_s) & \cdots & \nabla G(\mathbf{b}_N, \mathbf{r}_s) \cdot \nabla G(\mathbf{a}_M, \mathbf{r}_s) \end{pmatrix}. \tag{3.2}$$

Following previous work [11, 28, 29], we extract $\mathbf{r}_s \in D_s$ using two test vectors for each $\mathbf{r} \in \Omega$:

$$\mathbf{A}(\mathbf{r}) = \begin{pmatrix} \overline{G(\mathbf{a}_1, \mathbf{r})} & \overline{G(\mathbf{a}_2, \mathbf{r})} & \cdots & \overline{G(\mathbf{a}_M, \mathbf{r})} \end{pmatrix}$$
$$\mathbf{B}(\mathbf{r}) = \begin{pmatrix} \overline{G(\mathbf{b}_1, \mathbf{r})} & \overline{G(\mathbf{b}_2, \mathbf{r})} & \cdots & \overline{G(\mathbf{b}_N, \mathbf{r})} \end{pmatrix}$$

and introduce the corresponding normalized imaging function:

$$\mathfrak{F}(\mathbf{r}) = \frac{|\mathbf{B}(\mathbf{r})\mathbb{K}\mathbf{A}(\mathbf{r})^T|}{\max\limits_{\mathbf{r}\in\Omega} |\mathbf{B}(\mathbf{r})\mathbb{K}\mathbf{A}(\mathbf{r})^T|}.$$

Then, on the basis of [28], rings with large magnitudes centered at $\mathbf{r}_s$ will be included in the map of $\mathfrak{F}(\mathbf{r})$.

It is worth emphasizing that complete entries of $\mathbb{K}$ cannot be collected in a limited-aperture measurement configuration; specifically, for a fixed transmitter number m, only $N' = 49$ elements of scattered field data $u_{\text{scat}}(\mathbf{b}_n, \mathbf{a}_m)$, $n \in \Im_m = \{2m + p \pmod{72} : p = 11, 12, \ldots, 59\}$ are measurable. In order to treat unmeasurable scattered field data, motivated by several studies [17, 21, 36, 37], we convert the $N - \#(\Im_m) = N - N' = 23$ unknown data to zero and use the corresponding MSR matrix $\mathbb{M}$ with entries φ_{nm}, where

$$\varphi_{nm} = \begin{cases} u_{\text{scat}}(\mathbf{b}_n, \mathbf{a}_m), & n \in \Im_m \\ 0 & \text{otherwise.} \end{cases}$$

Fortunately, contrary to the previous research, it is possible to recognize the existence and location of D_s by using the following normalized imaging function.

$$\mathfrak{F}(\mathbf{r}) = \frac{|\mathbf{B}(\mathbf{r})\mathbb{M}\mathbf{A}(\mathbf{r})^T|}{\max\limits_{\mathbf{r}\in\Omega} |\mathbf{B}(\mathbf{r})\mathbb{M}\mathbf{A}(\mathbf{r})^T|} \quad \text{for each} \quad \mathbf{r} \in \Omega.$$

In order to explain the applicability of detection, we derive the following result:

Theorem 3.1. *For each $\mathbf{r} \in \Omega$, let $\mathbf{r} - \mathbf{r}_s = |\mathbf{r} - \mathbf{r}_s|(\cos\phi_s, \sin\phi_s)$ and assume that $k_{\text{b}}|\mathbf{r} - \mathbf{a}_m| \gg 0.25$ and $k_{\text{b}}|\mathbf{r} - \mathbf{b}_n| \gg 0.25$ for all $m = 1, 2, \ldots, M$ and $n = 1, 2, \ldots, N$. Then, $\mathfrak{F}(\mathbf{r})$ can be represented as*

$$\mathfrak{F}(\mathbf{r}) \approx \frac{|\Phi(\mathbf{r})|}{\max\limits_{\mathbf{r}\in\Omega} |\Phi(\mathbf{r})|}, \tag{3.3}$$

where

$$\Phi(\mathbf{r}) \approx \frac{441}{16|\mathbf{a}_m||\mathbf{b}_n|\pi} \sum_{s=1}^{S} \alpha_s^2 \left(\frac{\mu_{\text{b}}}{\mu_s + \mu_{\text{b}}}\right) \left[\frac{3\sqrt{3}}{2\pi} J_0(k_{\text{b}}|\mathbf{r} - \mathbf{r}_s|)^2 + \left(1 + \frac{3\sqrt{3}}{4\pi}\right) J_1(k_{\text{b}}|\mathbf{r} - \mathbf{r}_s|)^2 + \frac{3}{2\pi}\mathcal{E}(k_{\text{b}}|\mathbf{r} - \mathbf{r}_s|)\right]$$

and

$$\mathcal{E}(k_{\text{b}}|\mathbf{r} - \mathbf{r}_s|) = \sum_{p=2}^{\infty} \left(\frac{1}{1-p} \sin\frac{(1-p)\pi}{3} + \frac{1}{1+p} \sin\frac{(1+p)\pi}{3}\right) J_p(k_{\text{b}}|\mathbf{r} - \mathbf{r}_s|)^2.$$

Here, J_p denotes the Bessel function of the first kind of order p.

Proof. Since $k_{\text{b}}|\mathbf{r} - \mathbf{a}_m| \gg 0.25$ and $4k_{\text{b}}|\mathbf{r} - \mathbf{b}_n| \gg 1$ for $n = 1, 2, \cdots, N$, the following asymptotic forms hold (see [1, 34] for instance)

$$G(\mathbf{a}_m, \mathbf{r}) \approx -\frac{i(1-i)e^{ik_{\text{b}}|\mathbf{a}_m|}}{4\sqrt{k_{\text{b}}\pi|\mathbf{a}_m|}} e^{-ik_{\text{b}}\boldsymbol{\vartheta}_m\cdot\mathbf{r}} \quad \text{and} \quad \nabla G(\mathbf{a}_m, \mathbf{r}_s) \approx -\frac{ik_{\text{b}}(1-i)e^{ik_{\text{b}}|\mathbf{a}_m|}}{4\sqrt{k_{\text{b}}\pi|\mathbf{a}_m|}} \boldsymbol{\vartheta}_m e^{-ik_{\text{b}}\boldsymbol{\vartheta}_m\cdot\mathbf{r}_s}. \tag{3.4}$$

Thus, we can write

$$\mathbf{A}(\mathbf{r}) \approx \frac{(-1+i)e^{-ik_{\mathrm{b}}|\mathbf{a}_m|}}{4\sqrt{k_{\mathrm{b}}\pi|\mathbf{a}_m|}}\Big(e^{ik_{\mathrm{b}}\boldsymbol{\vartheta}_1\cdot\mathbf{r}} \quad e^{ik_{\mathrm{b}}\boldsymbol{\vartheta}_2\cdot\mathbf{r}} \quad \cdots \quad e^{ik_{\mathrm{b}}\boldsymbol{\vartheta}_M\cdot\mathbf{r}}\Big),$$

$$\mathbf{B}(\mathbf{r}) \approx \frac{(-1+i)e^{-ik_{\mathrm{b}}|\mathbf{b}_n|}}{4\sqrt{k_{\mathrm{b}}\pi|\mathbf{b}_n|}}\Big(e^{ik_{\mathrm{b}}\boldsymbol{\theta}_1\cdot\mathbf{r}} \quad e^{ik_{\mathrm{b}}\boldsymbol{\theta}_2\cdot\mathbf{r}} \quad \cdots \quad e^{ik_{\mathrm{b}}\boldsymbol{\theta}_N\cdot\mathbf{r}}\Big),$$

$$u_{\mathrm{scat}}(\mathbf{b}_n,\mathbf{a}_m) \approx \frac{ik_{\mathrm{b}}e^{ik_{\mathrm{b}}(|\mathbf{a}_m|+|\mathbf{b}_n|)}}{8\sqrt{|\mathbf{a}_m||\mathbf{b}_n|}}\sum_{s=1}^{S}\alpha_s^2\left(\frac{\mu_{\mathrm{b}}}{\mu_s+\mu_{\mathrm{b}}}\right)(\boldsymbol{\theta}_n\cdot\boldsymbol{\vartheta}_m)e^{-ik_{\mathrm{b}}(\boldsymbol{\theta}_n+\boldsymbol{\vartheta}_m)\cdot\mathbf{r}_s},$$

and correspondingly, we can evaluate

$$\mathbf{B}(\mathbf{r})\mathbb{M} = \frac{(1+i)k_{\mathrm{b}}e^{ik_{\mathrm{b}}|\mathbf{a}_m|}}{32|\mathbf{b}_n|\sqrt{k_{\mathrm{b}}\pi|\mathbf{a}_m|}}\begin{pmatrix} \sum_{s=1}^{S}\alpha_s^2\left(\frac{\mu_{\mathrm{b}}}{\mu_s+\mu_{\mathrm{b}}}\right)e^{-ik_{\mathrm{b}}\boldsymbol{\vartheta}_1\cdot\mathbf{r}_s}\sum_{n\in\Im(1)}(\boldsymbol{\theta}_n\cdot\boldsymbol{\vartheta}_1)e^{ik\boldsymbol{\theta}_n\cdot(\mathbf{r}-\mathbf{r}_s)} \\ \sum_{s=1}^{S}\alpha_s^2\left(\frac{\mu_{\mathrm{b}}}{\mu_s+\mu_{\mathrm{b}}}\right)e^{-ik_{\mathrm{b}}\boldsymbol{\vartheta}_2\cdot\mathbf{r}_s}\sum_{n\in\Im(2)}(\boldsymbol{\theta}_n\cdot\boldsymbol{\vartheta}_2)e^{ik\boldsymbol{\theta}_n\cdot(\mathbf{r}-\mathbf{r}_s)} \\ \vdots \\ \sum_{s=1}^{S}\alpha_s^2\left(\frac{\mu_{\mathrm{b}}}{\mu_s+\mu_{\mathrm{b}}}\right)e^{-ik_{\mathrm{b}}\boldsymbol{\vartheta}_M\cdot\mathbf{r}_s}\sum_{n\in\Im(m)}(\boldsymbol{\theta}_n\cdot\boldsymbol{\vartheta}_M)e^{ik\boldsymbol{\theta}_n\cdot(\mathbf{r}-\mathbf{r}_s)} \end{pmatrix}^T.$$

Since the following relations hold uniformly (e.g., see [11]):

$$e^{ix\cos\phi_s} = J_0(x) + \sum_{p=-\infty,p\neq 0}^{\infty} i^p J_p(x)e^{ip\phi_s} \tag{3.5}$$

and

$$\begin{aligned}\frac{1}{N}\sum_{n=1}^{N}(\boldsymbol{\theta}_n\cdot\boldsymbol{\xi})e^{ik_{\mathrm{b}}\boldsymbol{\theta}_n\cdot(\mathbf{r}-\mathbf{r}_s)} &\approx \frac{1}{\theta_N-\theta_1}\int_{\theta_1}^{\theta_N}\cos(\theta-\xi)e^{ik_{\mathrm{b}}|\mathbf{r}-\mathbf{r}_s|\cos(\theta-\phi_s)}\mathrm{d}\theta \\ &= \frac{2J_0(k_{\mathrm{b}}|\mathbf{r}-\mathbf{r}_s|)}{\theta_N-\theta_1}\sin\frac{\theta_N-\theta_1}{2}\cos\frac{\theta_N+\theta_1-2\xi}{2} + i\left(\frac{\mathbf{r}}{|\mathbf{r}|}\cdot\boldsymbol{\xi}\right)J_1(k_{\mathrm{b}}|\mathbf{r}-\mathbf{r}_s|) \\ &+ i\frac{J_1(k_{\mathrm{b}}|\mathbf{r}-\mathbf{r}_s|)}{\theta_N-\theta_1}\sin(\theta_N-\theta_1)\cos(\theta_N+\theta_1-\xi-\phi_s) \\ &+ \sum_{p=2}^{\infty}\frac{2i^pJ_p(k_{\mathrm{b}}|\mathbf{r}-\mathbf{r}_s|)}{\theta_N-\theta_1}\Big\{\frac{1}{1-p}\sin\frac{(1-p)(\theta_N-\theta_1)}{2}\cos\frac{(1-p)(\theta_N+\theta_1)+2p\phi_s-2\xi}{2} \\ &+ \frac{1}{1+p}\sin\frac{(1+p)(\theta_N-\theta_1)}{2}\cos\frac{(1+p)(\theta_N+\theta_1)-2p\phi_s-2\xi}{2}\Big\},\end{aligned} \tag{3.6}$$

it is possible to derive that

$$\frac{1}{N'}\sum_{n\in\Im(m)}(\boldsymbol{\theta}_n\cdot\boldsymbol{\vartheta}_m)e^{ik_{\mathrm{b}}\boldsymbol{\theta}_n\cdot(\mathbf{r}-\mathbf{r}_s)} \approx \frac{1}{5\pi/3-\pi/3}\int_{\vartheta_m+\pi/3}^{\vartheta_m+5\pi/3}\cos(\theta-\vartheta_m)e^{ik_{\mathrm{b}}|\mathbf{r}-\mathbf{r}_s|\cos(\theta-\phi_s)}\mathrm{d}\theta$$

$$= i\left(\frac{\mathbf{r}-\mathbf{r}_s}{|\mathbf{r}-\mathbf{r}_s|}\cdot\boldsymbol{\vartheta}_m\right)J_1(k_\mathrm{b}|\mathbf{r}-\mathbf{r}_s|) + \frac{3}{2\pi}J_1(k_\mathrm{b}|\mathbf{r}-\mathbf{r}_s|)\sin\frac{2\pi}{3}\cos(2\pi+2\vartheta_m-\vartheta_m-\phi_s) + \frac{3}{\pi}\Psi(\mathbf{r},\boldsymbol{\vartheta}_m)$$
$$= i\left(1+\frac{3\sqrt{3}}{4\pi}\right)\left(\frac{\mathbf{r}-\mathbf{r}_s}{|\mathbf{r}-\mathbf{r}_s|}\cdot\boldsymbol{\vartheta}_m\right)J_1(k_\mathrm{b}|\mathbf{r}-\mathbf{r}_s|) + \frac{3}{\pi}\Psi(\mathbf{r},\boldsymbol{\vartheta}_m) := i\Lambda(\boldsymbol{\vartheta}_m)J_1(k_\mathrm{b}|\mathbf{r}-\mathbf{r}_s|) + \frac{3}{\pi}\Psi(\mathbf{r},\boldsymbol{\vartheta}_m),$$

where

$$\Psi(\mathbf{r},\boldsymbol{\vartheta}_m) = -\frac{\sqrt{3}}{2}J_0(k_\mathrm{b}|\mathbf{r}-\mathbf{r}_s|) + \sum_{p=2}^{\infty} i^p J_p(k_\mathrm{b}|\mathbf{r}-\mathbf{r}_s|)\Big[\frac{1}{1-p}\sin\frac{(1-p)\pi}{3}\cos\left((1-p)\pi - p(\vartheta_m-\phi_s)\right)$$
$$+ \frac{1}{1+p}\sin\frac{(1+p)\pi}{3}\cos\left((1+p)\pi + p(\vartheta_m-\phi_s)\right)\Big].$$

Thus,

$$\mathbf{B}(\mathbf{r})\mathbb{M}\mathbf{A}(\mathbf{r})^T$$
$$= -\frac{N'}{64|\mathbf{a}_m||\mathbf{b}_n|\pi}\begin{pmatrix} \sum_{s=1}^{S}\alpha_s^2\left(\frac{\mu_\mathrm{b}}{\mu_s+\mu_\mathrm{b}}\right)e^{-ik_\mathrm{b}\boldsymbol{\vartheta}_1\cdot\mathbf{r}_s}\left[i\Lambda(\boldsymbol{\vartheta}_1)J_1(k_\mathrm{b}|\mathbf{r}-\mathbf{r}_s|)+\frac{3}{\pi}\Psi(\mathbf{r},\boldsymbol{\vartheta}_1)\right] \\ \sum_{s=1}^{S}\alpha_s^2\left(\frac{\mu_\mathrm{b}}{\mu_s+\mu_\mathrm{b}}\right)e^{-ik_\mathrm{b}\boldsymbol{\vartheta}_2\cdot\mathbf{r}_s}\left[i\Lambda(\boldsymbol{\vartheta}_2)J_1(k_\mathrm{b}|\mathbf{r}-\mathbf{r}_s|)+\frac{3}{\pi}\Psi(\mathbf{r},\boldsymbol{\vartheta}_2)\right] \\ \vdots \\ \sum_{s=1}^{S}\alpha_s^2\left(\frac{\mu_\mathrm{b}}{\mu_s+\mu_\mathrm{b}}\right)e^{-ik_\mathrm{b}\boldsymbol{\vartheta}_M\cdot\mathbf{r}_s}\left[i\Lambda(\boldsymbol{\vartheta}_M)J_1(k_\mathrm{b}|\mathbf{r}-\mathbf{r}_s|)+\frac{3}{\pi}\Psi(\mathbf{r},\boldsymbol{\vartheta}_M)\right] \end{pmatrix}^T \begin{pmatrix} e^{ik_\mathrm{b}\boldsymbol{\vartheta}_1\cdot\mathbf{r}} \\ e^{ik_\mathrm{b}\boldsymbol{\vartheta}_2\cdot\mathbf{r}} \\ \vdots \\ e^{ik_\mathrm{b}\boldsymbol{\vartheta}_M\cdot\mathbf{r}} \end{pmatrix}$$
$$= -\frac{49\cdot 9}{16|\mathbf{a}_m||\mathbf{b}_n|\pi}\sum_{s=1}^{S}\alpha_s^2\left(\frac{\mu_\mathrm{b}}{\mu_s+\mu_\mathrm{b}}\right)\left[\frac{1}{M}\sum_{m=1}^{M}e^{ik_\mathrm{b}\boldsymbol{\vartheta}_m\cdot(\mathbf{r}-\mathbf{r}_s)}\left(i\Lambda(\boldsymbol{\vartheta}_m)J_1(k_\mathrm{b}|\mathbf{r}-\mathbf{r}_s|)+\frac{3}{\pi}\Psi(\mathbf{r},\boldsymbol{\vartheta}_m)\right)\right].$$

Reapplying (3.6), we have

$$\frac{1}{M}\sum_{m=1}^{M}\left(\frac{\mathbf{r}-\mathbf{r}_s}{|\mathbf{r}-\mathbf{r}_s|}\cdot\boldsymbol{\vartheta}_m\right)e^{ik_\mathrm{b}\boldsymbol{\vartheta}_m\cdot(\mathbf{r}-\mathbf{r}_s)}J_1(k_\mathrm{b}|\mathbf{r}-\mathbf{r}_s|) \approx \frac{1}{2\pi}\int_{\mathbb{S}^1}\left(\frac{\mathbf{r}-\mathbf{r}_s}{|\mathbf{r}-\mathbf{r}_s|}\cdot\boldsymbol{\vartheta}\right)e^{ik_\mathrm{b}\boldsymbol{\vartheta}\cdot(\mathbf{r}-\mathbf{r}_s)}J_1(k_\mathrm{b}|\mathbf{r}-\mathbf{r}_s|)\mathrm{d}\boldsymbol{\vartheta}$$
$$= i\left(\frac{\mathbf{r}-\mathbf{r}_s}{|\mathbf{r}-\mathbf{r}_s|}\cdot\frac{\mathbf{r}-\mathbf{r}_s}{|\mathbf{r}-\mathbf{r}_s|}\right)J_1(k_\mathrm{b}|\mathbf{r}-\mathbf{r}_s|)^2 = iJ_1(k_\mathrm{b}|\mathbf{r}-\mathbf{r}_s|)^2.$$

Furthermore, since

$$\frac{1}{M}\sum_{m=1}^{M}e^{ik_\mathrm{b}\boldsymbol{\vartheta}_m\cdot(\mathbf{r}-\mathbf{r}_s)}J_0(k_\mathrm{b}|\mathbf{r}-\mathbf{r}_s|) \approx \frac{1}{2\pi}\int_{\mathbb{S}^1}e^{ik_\mathrm{b}\boldsymbol{\vartheta}\cdot(\mathbf{r}-\mathbf{r}_s)}J_0(k_\mathrm{b}|\mathbf{r}-\mathbf{r}_s|)\mathrm{d}\boldsymbol{\vartheta} = J_0(k_\mathrm{b}|\mathbf{r}-\mathbf{r}_s|)^2,$$
$$\frac{1}{M}\sum_{m=1}^{M}e^{ik_\mathrm{b}\boldsymbol{\vartheta}_m\cdot(\mathbf{r}-\mathbf{r}_s)}\cos\left((1-p)\pi-p(\vartheta_m-\phi_s)\right) \approx \frac{1}{2\pi}\int_0^{2\pi}e^{ik_\mathrm{b}|\mathbf{r}-\mathbf{r}_s|\cos(\vartheta-\phi_s)}\cos\left((1-p)\pi-p(\vartheta-\phi_s)\right)d\vartheta$$
$$= \frac{1}{2\pi}\int_0^{2\pi}\left(J_0(k_\mathrm{b}|\mathbf{r}-\mathbf{r}_s|)+\sum_{q=-\infty,q\neq 0}^{\infty}i^qJ_q(k_\mathrm{b}|\mathbf{r}-\mathbf{r}_s|)e^{iq(\vartheta-\phi_s)}\right)\cos\left(p(\vartheta-\phi_s)+(1-p)\pi\right)d\vartheta$$

$$= \frac{i^p}{2} J_p(k_b|\mathbf{r}-\mathbf{r}_s|)\cos\left((1-p)\pi\right) = \frac{(-1)^{p-1}i^p}{2} J_p(k_b|\mathbf{r}-\mathbf{r}_s|)$$

and

$$\frac{1}{M}\sum_{m=1}^{M} e^{ik_b\boldsymbol{\vartheta}_m\cdot(\mathbf{r}-\mathbf{r}_s)}\cos\left((1+p)\pi + p(\vartheta_m-\phi_s)\right) \approx \frac{i^p}{2} J_p(k_b|\mathbf{r}-\mathbf{r}_s|)\cos\left((1+p)\pi\right) = \frac{(-1)^{p+1}i^p}{2} J_p(k_b|\mathbf{r}-\mathbf{r}_s|),$$

we can obtain

$$\begin{aligned}\frac{1}{M}\sum_{m=1}^{M} e^{ik_b\boldsymbol{\vartheta}_m\cdot(\mathbf{r}-\mathbf{r}_s)}\left(i\Lambda(\boldsymbol{\vartheta}_m)J_1(k_b|\mathbf{r}-\mathbf{r}_s|) + \frac{3}{2\pi}\Psi(\mathbf{r},\boldsymbol{\vartheta}_m)\right) \approx -\left(1+\frac{3\sqrt{3}}{4\pi}\right)J_1(k_b|\mathbf{r}-\mathbf{r}_s|)^2 \\ -\frac{\sqrt{3}}{2}J_0(k_b|\mathbf{r}-\mathbf{r}_s|)^2 - \frac{1}{2}\sum_{p=2}^{\infty}\left(\frac{1}{1-p}\sin\frac{(1-p)\pi}{3} + \frac{1}{1+p}\sin\frac{(1+p)\pi}{3}\right)J_p(k_b|\mathbf{r}-\mathbf{r}_s|)^2,\end{aligned}$$

and correspondingly (3.3) can be derived. □

Based on the result of Theorem 3.1, we can explore some undiscovered properties of the imaging function.

Remark 3.1 (Detectability of objects). Following the previous studies, the main component of the imaging function in TE polarization is $J_1(k_b|\mathbf{r}-\mathbf{r}_s|)^2$. Therefore, rings of large magnitude appeared in the imaging results. Contrary to the previous studies, the imaging function $\mathfrak{F}(\mathbf{r})$ is composed of $J_0(k_b|\mathbf{r}-\mathbf{r}_s|)^2$, $J_1(k_b|\mathbf{r}-\mathbf{r}_s|)^2$, and $\mathcal{E}(k_b|\mathbf{r}-\mathbf{r}_s|)$. Hence, the local maxima of $\mathfrak{F}(\mathbf{r})$ will appear at the location of the object because $J_0(0) = 1$ and $J_p(0) = 0$ for nonzero p. This is the theoretical reason that, unlike the previous studies, the existence and outline shape of objects can be identified through the map $\mathfrak{F}(\mathbf{r})$.

Remark 3.2 (Material properties). Since

$$\mathfrak{F}(\mathbf{r}_s) \propto \alpha_s^2\left(\frac{\mu_b}{\mu_s+\mu_b}\right),$$

the value of $\mathfrak{F}(\mathbf{r})$ should depend on the size and permeability of objects. For example, if the sizes of the objects are the same and $\mu_s > \mu_{s'}$, then $\mathfrak{F}(\mathbf{r}_s) < \mathfrak{F}(\mathbf{r}_{s'})$. Correspondingly, if the size or permeability of an object D_s is extremely smaller or greater than the one of another object $D_{s'}$, the existence of D_s cannot be recognized through the map of $\mathfrak{F}(\mathbf{r})$ because $\mathfrak{F}(\mathbf{r}_s) \ll \mathfrak{F}(\mathbf{r}_{s'})$.

Remark 3.3 (Applied frequencies and image resolution). The resolution of $\mathfrak{F}(\mathbf{r})$ is highly dependent on the value of k_b. Based on the property of the J_0, an image with high resolution can be obtained if one applies a high frequency, but several artifacts are also included. If one applies a low frequency, an image with low resolution will be obtained. We refer to Figure 2 for 1D plots of $J_0(k_b|x|)$ with several frequencies.

Notice that as $J_1(x)$ is maximized at $x \approx 3.8317$, the two large-magnitude peaks appear at

$$\mathbf{r} \approx \mathbf{r}_s \pm \frac{3.8317}{k_b}.$$

That is, two peaks will converge to the location of D at sufficiently high frequency, and correspondingly, it will be possible to recognize not only the existence but also the outline shape of objects. We refer to Figure 3 and Example 4.2.

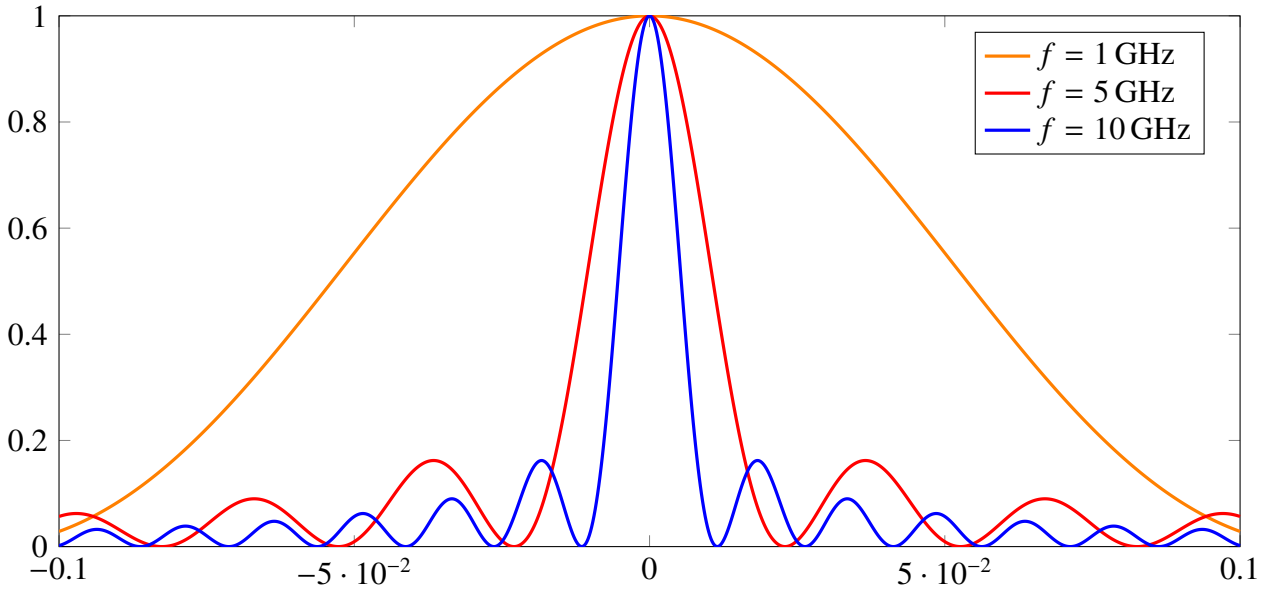

Figure 2. Plots of $J_0(k_b|x|)^2$ for $-0.1 \le x \le 0.1$ at $f = 1, 5, 10$ GHz.

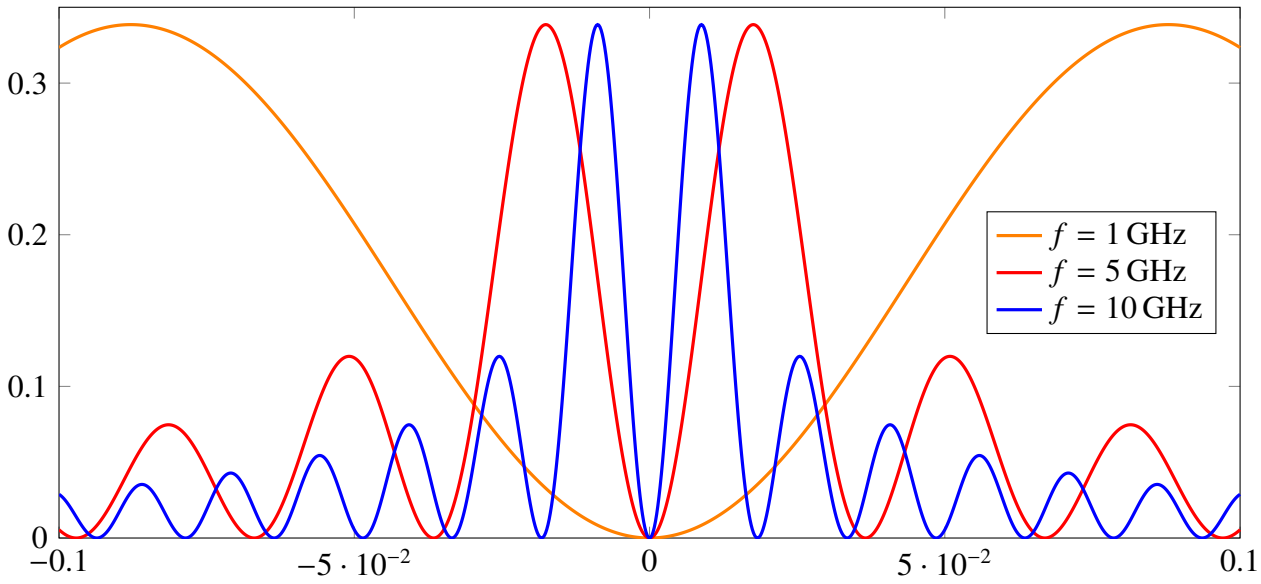

Figure 3. Plots of $J_1(k_b|x|)^2$ for $-0.1 \le x \le 0.1$ at $f = 1, 5, 10$ GHz.

4. Numerical simulation results using synthetic and experimental data

In this section, we support Theorem 3.1 through numerical simulations on synthetic and experimental data. For the synthetic data experiment, we set three small circles D_s, $s = 1, 2, 3$, with radius α_s, permittivity ε_b, permeability μ_s, and locations $\mathbf{r}_1 = (0.07\,\text{m}, 0.05\,\text{m})$, $\mathbf{r}_2 = (-0.07\,\text{m}, 0.00\,\text{m})$, and $\mathbf{r}_3 = (0.04\,\text{m}, -0.06\,\text{m})$. Table 1 lists the parameter values of the four experimental cases. The antenna arrangements and other simulation configurations are those specified

in [33], and the search domain Ω was chosen as a square region $[-0.1\,\text{m}, 0.1\,\text{m}] \times [-0.1\,\text{m}, 0.1\,\text{m}]$. Within this setting, maps of $\mathfrak{F}(\mathbf{r})$ were obtained at frequencies of $f = 4, 8, 12\,\text{GHz}$.

Table 1. Permeabilities and sizes of objects in synthetic data experiment.

	μ_1	μ_2	μ_3	α_1	α_2	α_3
Case 1	$5\mu_b$	$5\mu_b$	$5\mu_b$	0.1 m	0.1 m	0.1 m
Case 2	$3\mu_b$	$5\mu_b$	$7\mu_b$	0.1 m	0.1 m	0.1 m
Case 3	$5\mu_b$	$5\mu_b$	$5\mu_b$	0.15 m	0.1 m	0.05 m
Case 4	$3\mu_b$	$5\mu_b$	$7\mu_b$	0.15 m	0.1 m	0.05 m

Example 4.1 (Results of the synthetic data). Figure 4 shows maps of $\mathfrak{F}(\mathbf{r})$ in Case 1. Although the existence and locations of D_s can be identified in the imaging results, the outline shapes are indistinguishable. Similarly, the existence and locations of D_s in the imaging results of Case 2 with different μ_s values are discernible, but the outline shapes are obscured (see Figure 5).

Figure 6 shows the imaging results of Case 3. Here, D_3 cannot be recognized because it is much smaller than D_1 (i.e., $\alpha_1^2 \gg \alpha_3^2$). Therefore, $\mathfrak{F}(\mathbf{r})$ in the neighborhood of D_3 is very much smaller than $\mathfrak{F}(\mathbf{r})$ in the neighborhood of D_1.

Figure 7 shows maps of $\mathfrak{F}(\mathbf{r})$ in Case 4. Since

$$\alpha_1^2\left(\frac{\mu_b}{\mu_1+\mu_b}\right) = 0.0056 > \alpha_2^2\left(\frac{\mu_b}{\mu_2+\mu_b}\right) = 0.0017 \gg \alpha_3^2\left(\frac{\mu_b}{\mu_3+\mu_b}\right) = 3.1250\times 10^{-4},$$

$\mathfrak{F}(\mathbf{r})$ in the neighborhood of D_1 is considerably larger than $\mathfrak{F}(\mathbf{r})$ in the neighborhoods of D_2 and D_3. Correspondingly, D_3 cannot be recognized, and D_2 is barely recognizable.

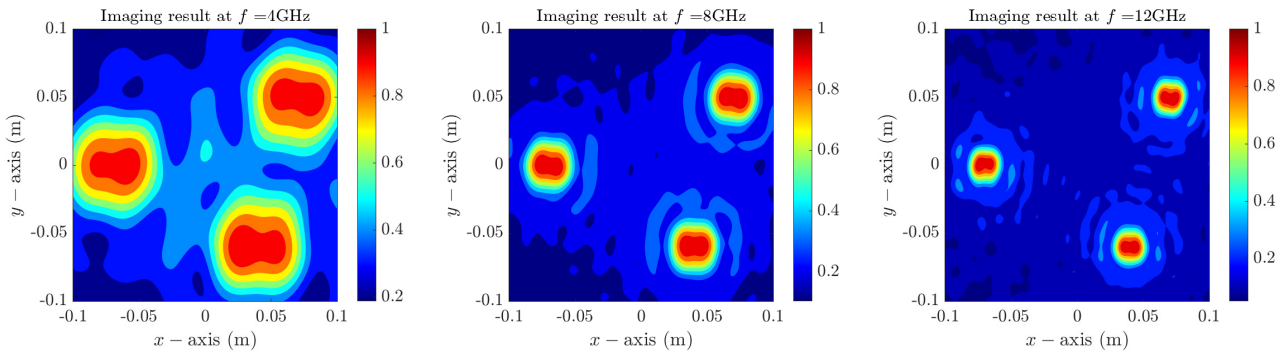

Figure 4. Maps of $\mathfrak{F}(\mathbf{r})$ in Case 1.

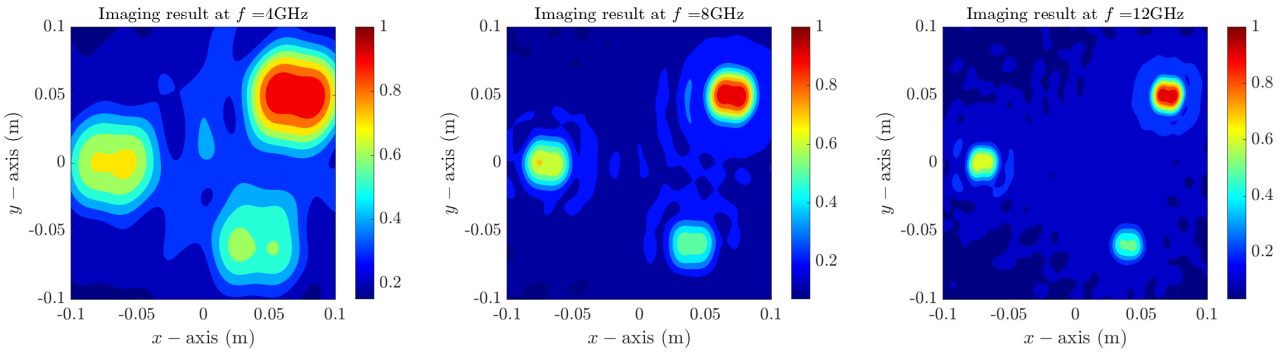

Figure 5. Maps of $\mathfrak{F}(\mathbf{r})$ in Case 2.

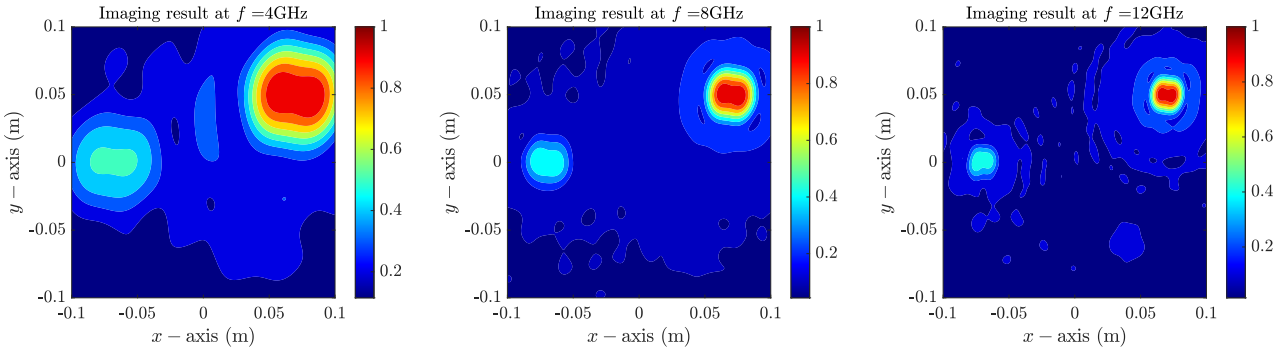

Figure 6. Maps of $\mathfrak{F}(\mathbf{r})$ in Case 3.

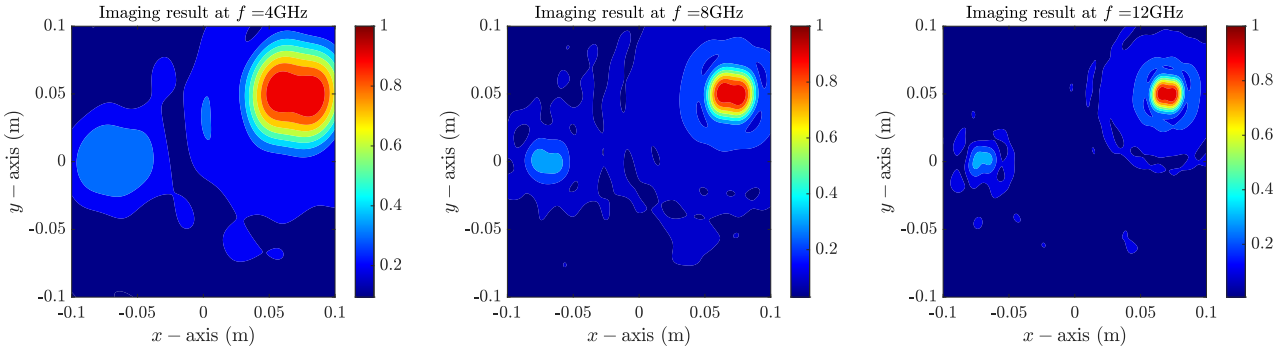

Figure 7. Maps of $\mathfrak{F}(\mathbf{r})$ in Case 4.

Example 4.2 (Results of the experimental data). Figure 8 shows the $\mathfrak{F}(\mathbf{r})$ maps of a metallic rectangle D from the dataset '`rectTE_8f.exp`' from [33]. At $f = 4\,\text{GHz}$ and $f = 8\,\text{GHz}$, the imaging results display a large-magnitude peak at the location of D and two large-magnitude peaks in the normal direction of D. Notice that, as we discussed in Remark 3.3, we can recognize not only the existence but also the outline shape of object D through the map of $\mathfrak{F}(\mathbf{r})$ with high frequency $f = 12\,\text{GHz}$.

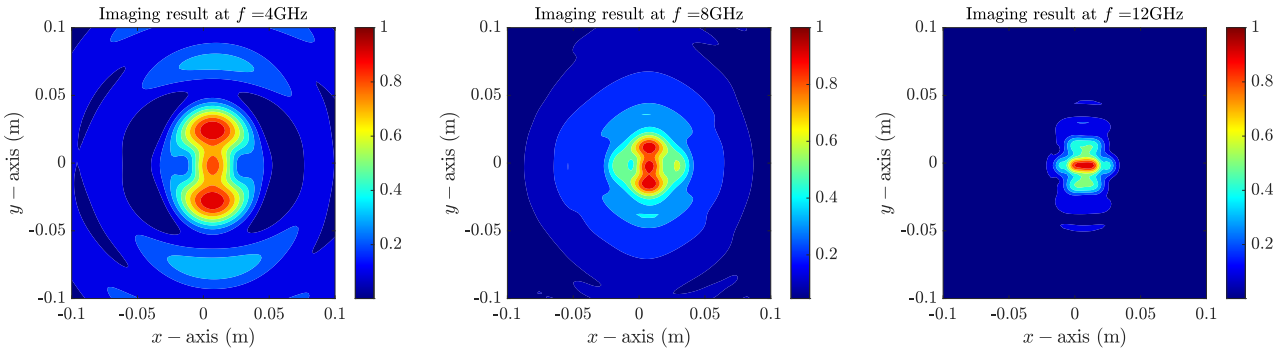

Figure 8. Maps of $\mathfrak{F}(\mathbf{r})$ on Fresnel experimental data.

5. Conclusions

We applied KM for fast identification of the existence and locations of small objects in transverse electric polarization. By considering the relationship between the imaging function and the squared zero-order and first-order Bessel functions and an infinite series of Bessel functions of order greater than two, we also explored various properties (including the possibility of object detection) of the KM. From the simulation results of synthetic and Fresnel experimental data, we concluded that the KM algorithm effectively detects small objects in transverse electric polarization scenarios.

Although the existence and approximate locations of objects can be retrieved, the locations and outline shapes of objects are not satisfactorily resolved. An improved imaging technique will be developed in forthcoming work. The current study focused on the retrieval of small 2D objects. Extension to the three-dimensional problem on a dataset [38] will be an interesting research topic.

Author contributions

Junyong Eom: Formal analysis, Methodology, Writing - original draft, Writing - review & editing, Funding acquisition; Won-Kwang Park: Conceptualization, Formal analysis, Investigation, Software, Validation, Writing - original draft, Writing - review & editing, Funding acquisition. All authors have read and agreed to the published version of the manuscript.

Use of AI tools declaration

The authors declare that no Artificial Intelligence (AI) tools were used in the creation of this article.

Acknowledgements

This study was supported by the JSPS KAKENHI (Grant Number 23K19002) and National Research Foundation of Korea (NRF) grant funded by the Korea government (MSIT) (NRF-2020R1A2C1A01005221).

Conflict of interest

The authors declare no conflicts of interest regarding the publication of this paper.

References

1. S. Kang, W.-K. Park, A novel study on the bifocusing method in two-dimensional inverse scattering problem, *AIMS Mathematics*, **8** (2023), 27080–27112. https://doi.org/10.3934/math.20231386
2. S. Kang, W.-K. Park, S.-H. Son, A qualitative analysis of the bifocusing method for a real-time anomaly detection in microwave imaging, *Comput. Math. Appl.*, **137** (2023), 93–101. https://doi.org/10.1016/j.camwa.2023.02.017
3. Y. J. Kim, L. Jofre, F. D. Flaviis, M. Q. Feng, Microwave reflection tomographic array for damage detection of civil structures, *IEEE Trans. Antennas Propag.*, **51** (2003), 3022–3032. https://doi.org/10.1109/TAP.2003.818786
4. K. Ito, B. Jin, J. Zou, A direct sampling method to an inverse medium scattering problem, *Inverse Probl.*, **28** (2012), 025003. https://doi.org/10.1088/0266-5611/28/2/025003
5. S. Kang, M. Lambert, W.-K. Park, Analysis and improvement of direct sampling method in the mono-static configuration, *IEEE Geosci. Remote Sens. Lett.*, **16** (2019), 1721–1725. https://doi.org/10.1109/LGRS.2019.2906366
6. W.-K. Park, Direct sampling method for retrieving small perfectly conducting cracks, *J. Comput. Phys.*, **373** (2018), 648–661. https://doi.org/10.1016/j.jcp.2018.07.014
7. H. Ammari, E. Iakovleva, D. Lesselier, A MUSIC algorithm for locating small inclusions buried in a half-space from the scattering amplitude at a fixed frequency, *Multiscale Model. Simul.*, **3** (2005), 597–628. https://doi.org/10.1137/040610854
8. W.-K. Park, Application of MUSIC algorithm in real-world microwave imaging of unknown anomalies from scattering matrix, *Mech. Syst. Signal Proc.*, **153** (2021), 107501. https://doi.org/10.1016/j.ymssp.2020.107501
9. W.-K. Park, A novel study on the MUSIC-type imaging of small electromagnetic inhomogeneities in the limited-aperture inverse scattering problem, *J. Comput. Phys.*, **460** (2022), 111191. https://doi.org/10.1016/j.jcp.2022.111191
10. H. Ammari, J. Garnier, H. Kang, W.-K. Park and K. Sølna, Imaging schemes for perfectly conducting cracks, *SIAM J. Appl. Math.*, **71** (2011), 68–91. https://doi.org/10.1137/100800130
11. W.-K. Park, Multi-frequency subspace migration for imaging of perfectly conducting, arc-like cracks in full- and limited-view inverse scattering problems, *J. Comput. Phys.*, **283** (2015), 52–80. https://doi.org/10.1016/j.jcp.2014.11.036
12. W.-K. Park, On the identification of small anomaly in microwave imaging without homogeneous background information, *AIMS Mathematics*, **8** (2023), 27210–27226. https://doi.org/10.3934/math.20231392
13. A. Carpio, M. Pena, M.-L. Rapún, Processing the 2D and 3D Fresnel experimental databases via topological derivative methods, *Inverse Probl.*, **37** (2021), 105012. https://doi.org/10.1088/1361-6420/ac21c8

14. J. F. Funes, J. M. Perales, M.-L. Rapún, J. M. Vega, Defect detection from multi-frequency limited data via topological sensitivity, *J. Math. Imaging Vis.*, **55** (2016), 19–35. https://doi.org/10.1007/s10851-015-0611-y

15. W.-K. Park, Topological derivative strategy for one-step iteration imaging of arbitrary shaped thin, curve-like electromagnetic inclusions, *J. Comput. Phys.*, **231** (2012), 1426–1439. https://doi.org/10.1016/j.jcp.2011.10.014

16. L. Audibert, H. Haddar, The generalized linear sampling method for limited aperture measurements, *SIAM J. Imaging Sci.*, **10** (2017), 845–870. https://doi.org/10.1137/16M110112X

17. P. Monk, M. Pena, V. Selgas, Multifrequency linear sampling method on experimental datasets, *IEEE Trans. Antennas Propag.*, **71** (2023), 8788–8798. https://doi.org/10.1109/TAP.2023.3298974

18. G. Bozza, M. Brignone, M. Pastorino, Application of the no-sampling linear sampling method to breast cancer detection, *IEEE Trans. Biomed. Eng.*, **57** (2010), 2525–2534. https://doi.org/10.1109/tbme.2010.2055059

19. M. T. Bevacqua, T. Isernia, R. Palmeri, M. N. Akinci, L. Crocco, Physical insight unveils new imaging capabilities of orthogonality sampling method, *IEEE Trans. Antennas Propag.*, **68** (2020), 4014–4021. https://doi.org/10.1109/TAP.2019.2963229

20. I. Harris, D.-L. Nguyen, Orthogonality sampling method for the electromagnetic inverse scattering problem, *SIAM J. Sci. Comput.*, **42** (2020), B722–B737. https://doi.org/10.1137/19M129783X

21. W.-K. Park, On the application of orthogonality sampling method for object detection in microwave imaging, *IEEE Trans. Antennas Propag.*, **71** (2023), 934–946. https://doi.org/10.1109/TAP.2022.3220033

22. A. Alzaalig, G. Hu, X. Liu, J. Sun, Fast acoustic source imaging using multi-frequency sparse data, *Inverse Probl.*, **36** (2020), 025009. https://doi.org/10.1088/1361-6420/ab4aec

23. H. Ammari, S. Moskow, M. Vogelius, Boundary integral formulae for the reconstruction of electric and electromagnetic inhomogeneities of small volume, *ESAIM: COCV*, **9** (2003), 49–66. https://doi.org/10.1051/cocv:2002071

24. M. Brühl, M. Hanke, M. Pidcock, Crack detection using electrostatic measurements, *ESAIM: Math. Model. Numer. Anal.*, **35** (2001), 595–605. https://doi.org/10.1051/m2an:2001128

25. N. Simonov, B.-R. Kim, K.-J. Lee, S.-I. Jeon, S.-H. Son, Advanced fast 3-D electromagnetic solver for microwave tomography imaging, *IEEE Trans. Med. Imag.*, **36** (2017), 2160–2170. https://doi.org/10.1109/TMI.2017.2712800

26. S.-H. Son, K.-J. Lee, W.-K. Park, Application and analysis of direct sampling method in real-world microwave imaging, *Appl. Math. Lett.*, **96** (2019), 47–53. https://doi.org/10.1016/j.aml.2019.04.016

27. S.-H. Son, K.-J. Lee, W.-K. Park, Real-time tracking of moving objects from scattering matrix in real-world microwave imaging, *AIMS Math.*, **9** (2024), 13570–13588. https://doi.org/10.3934/math.2024662

28. S. Hou, K. Sølna, H. Zhao, A direct imaging algorithm for extended targets, *Inverse Probl.*, **22** (2006), 1151–1178. https://doi.org/10.1088/0266-5611/22/4/003

29. W.-K. Park, Asymptotic properties of MUSIC-type imaging in two-dimensional inverse scattering from thin electromagnetic inclusions, *SIAM J. Appl. Math.*, **75** (2015), 209–228. https://doi.org/10.1137/140975176

30. W.-K. Park, Detection of small inhomogeneities via direct sampling method in transverse electric polarization, *Appl. Math. Lett.*, **79** (2018), 169–175. https://doi.org/10.1016/j.aml.2017.12.016

31. W.-K. Park, Shape identification of open sound-hard arcs without priori information in limited-view inverse scattering problem, *Comput. Math. Appl.*, **128** (2022), 55–68. https://doi.org/10.1016/j.camwa.2022.10.010

32. M.-L. Rapún, On the solution of direct and inverse multiple scattering problems for mixed sound-soft, sound-hard and penetrable objects, *Inverse Probl.*, **36** (2020), 095014. https://doi.org/10.1088/1361-6420/ab98a2

33. K. Belkebir, M. Saillard, Special section: Testing inversion algorithms against experimental data, *Inverse Probl.*, **17** (2001), 1565–1571. https://doi.org/10.1088/0266-5611/21/6/S01

34. D. Colton, R. Kress, *Inverse Acoustic and Electromagnetic Scattering Problems*, 2 Eds., Berlin, Heidelberg: Springer, 1998.

35. H. Ammari, H. Kang, *Reconstruction of Small Inhomogeneities from Boundary Measurements*, Berlin, Heidelberg: Springer, 2004. https://doi.org/10.1007/b98245

36. L. Crocco, I. Catapano, L. D. Donato, T. Isernia, The linear sampling method as a way to quantitative inverse scattering, *IEEE Trans. Antennas Propag.*, **60** (2012), 1844–1853. https://doi.org/10.1109/TAP.2012.2186250

37. W.-K. Park, On the application of subspace migration from scattering matrix with constant-valued diagonal elements in microwave imaging, *AIMS Mathematics*, **9** (2024), 21356–21382. https://doi.org/10.3934/math.20241037

38. J.-M. Geffrin, P. Sabouroux, C. Eyraud, Free space experimental scattering database continuation: Experimental set-up and measurement precision, *Inverse Probl.*, **21** (2005), S117–S130. https://doi.org/10.1088/0266-5611/21/6/S09

AIMS Press